Original Paper

phys. stat. sol. (a) **202**, No. 12, 2249–2266 (2005) / **DOI** 10.1002/pssa.200521262

Plastic deformation of $MoSi_2$ single crystals along ⟨110⟩

Christian Dietzsch, Martin Bartsch, and **Ulrich Messerschmidt***

Max-Planck-Institut für Mikrostrukturphysik, Weinberg 2, 06120 Halle/Saale, Germany

Received 1 June 2005, revised 24 August 2005, accepted 24 August 2005
Published online 12 September 2005

Dedicated to Professor Dr. Johannes Heydenreich on the occasion of his 75th birthday

PACS 61.72.Ff, 61.72.Lk, 62.20.Fe, 68.37.Lp, 81.40.Lm

$MoSi_2$ single crystals were deformed along the soft ⟨110⟩ compression axis between room temperature and 1050 °C. The strain rate sensitivity of the flow stress was determined by stress relaxation tests. The temperature dependence of the flow stress shows three temperature ranges, a low and a high-temperature range with a normal decrease of the flow stress with increasing temperature and an intermediate range with an anomalous flow stress increase. In the latter range, the strain rate sensitivity decreases (inversely) with increasing strain rate. The dislocation structures of the deformed samples were imaged in diffraction contrast in a high-voltage electron microscope. In contrast to the low and high-temperature ranges, the dislocations are straight and oriented along ⟨111⟩ directions in the anomaly range. The results are interpreted by a large athermal stress component, the action of the Peierls mechanism in the low temperature range, a new dissociation model of the dislocations requiring conservative climb in the dislocation core in the anomaly range, and recovery-controlled deformation in the high-temperature range.

1 Introduction

Materials based on molybdenum disilicide are promising for structural applications at high temperatures because of their relatively high flow stress and good oxidation resistance above 1000 °C. $MoSi_2$ has the tetragonal $C11_b$ structure with a high c/a ratio close to $\sqrt{6}$. This implies strong plastic anisotropy with a number of slip systems. In the first studies on single crystals, plastic deformation was achieved only above 900 °C [1–4]. The slip systems observed are {110} 1/2⟨111⟩, {011} ⟨100⟩, {010} ⟨100⟩, {110} 1/2⟨331⟩, {013} 1/2⟨331⟩, and {011} 1/2⟨111⟩. The first four systems have zero orientation factors for loading along [001]. In a thorough study of the orientation dependence of the plastic properties, it was found that $MoSi_2$ can be deformed plastically even down to room temperature and lower along orientations away from [001] [5]. In these soft orientations, there appears a flow stress anomaly, i.e. an anomalous increase of the flow stress with increasing temperature in different ranges between about 600 °C and 1100 °C, depending on the orientation. The temperature dependence of the critical resolved shear stress of most of the slip systems listed above was obtained from the data and from studies of the slip lines on the surfaces and transmission electron microscopy determination of the Burgers vectors.

The flow stress anomaly is a desired property. In the literature, several mechanisms have been proposed which may control the dislocation mobility and lead to the anomaly in $MoSi_2$.

– Dissociation of dislocations on planes different from the easy slip plane in analogy to the Kear–Wilsdorf locks in $L1_2$ intermetallic alloys [6–8]. This mechanism was proposed for dislocations with 1/2⟨331⟩ Burgers vectors with cross-slip from the {110} slip plane onto the {013} plane [1]. According

* Corresponding author: e-mail: um@mpi-halle.de, Phone: +49 345 5582 927, Fax: +49 345 5511223

to [9], the fault energy should be higher on {013} than on {110} so that this mechanism should not be probable.

– It is quite established [5, 10] that dislocations on the easy slip system {110} 1/2⟨111⟩ are dissociated according to

$$1/2\langle 111\rangle = 1/4\langle 111\rangle + \mathrm{SISF} + 1/4\langle 111\rangle\,, \tag{1}$$

where SISF stands for a superlattice intrinsic stacking fault.

– Addition of solutes to $MoSi_2$ may result in both hardening or softening, depending on whether the respective additions form disilicides with the $C11_b$ or the C40 structure [11]. The interpretation is based on a Peierls model of the dislocation dissociated according to Eq. (1) with the solutes influencing the stacking fault energy, thus changing the core structure and accordingly the Peierls stress.

– Another explanation of the solute hardening and softening effects is the assumption that the solutes influence the kink-pair properties on the leading partial dislocation [12–14]. A reduction of the kink-pair formation energy may lead to softening at lower temperatures while kink migration may be hindered at high temperatures resulting in solution hardening.

– In some orientations, $MoSi_2$ shows serrated flow (e.g., [5]), which was interpreted at first by strain ageing in [5], i.e., by diffusive processes of solutes in the field of the moving dislocations like the Cottrell effect [15]. Since the impurity concentrations in the $MoSi_2$ single crystals are mostly too low for this effect, a model was suggested in which dislocations form a configuration of lowest energy which requires a certain number of intrinsic point defects in their core, and that this configuration moves along with the dislocations resulting in a friction like a Cottrell cloud [16].

The assumption that, in the range of the flow stress anomaly, the dislocation mobility in $MoSi_2$ is controlled by processes with kinetics like the Cottrell effect is very attractive since it explains the dynamic behaviour of dislocations observed during *in situ* straining experiments in a transmission electron microscope along the soft ⟨201⟩ orientation, where the {110} 1/2⟨111⟩ slip system is activated [16–18]. During first loading, many dislocations are generated and move almost instantaneously. Later on, they move in a smooth viscous way. Cottrell effect-type kinetics are also consistent with an inverse dependence of the strain rate sensitivity of the flow stress on the strain rate itself, i.e., a decrease of the strain rate sensitivity with increasing strain rate or stress [18]. These observations are typical also for some other intermetallic alloys showing a flow stress anomaly. During the deformation of $MoSi_2$ single crystals along the soft ⟨201⟩ orientation, dislocations with 1/2⟨111⟩ Burgers vectors are very straight and oriented along crystallographic directions. The orientation changes from 60° character along ⟨111⟩ at low temperatures to ⟨110⟩ and ⟨331⟩ (60° and edge characters) within the anomaly range [19–21]. The 60° ⟨111⟩ and ⟨110⟩ orientations are crystallographically not equivalent. The occurrence of the straight dislocations oriented along ⟨110⟩ in the anomaly range was interpreted in analogy to the model in [22] for dislocations with ⟨110⟩ Burgers vectors in NiAl. The dislocations dissociate by glide on planes different from the glide plane of the total dislocation. The dissociated dislocation can move along its glide plane only by a combination of glide and conservative climb of the partial dislocations, i.e., one partial dislocation absorbs the vacancies produced by the other one. For the dislocations with 1/2⟨111⟩ Burgers vectors in $MoSi_2$ along ⟨110⟩, a possible dissociation is [21]

$$1/2[111]\,(1\bar{1}0) \rightarrow 1/6[331]\,(1\bar{1}0) + 1/6[3\bar{3}1]\,(\bar{1}16) + 1/6[\bar{3}31]\,(1\bar{1}6)\,. \tag{2}$$

Using anisotropic elasticity theory, the reaction is accompanied by a gain in elastic energy of about 3%. The three glide planes of the partial dislocations intersect along the [110] preference direction of the total dislocation. This is the constraint leading to the straight oriented shape of the dislocations. According to [23], the energy of the APB fault on the $(1\bar{1}0)$ plane is very high so that the dissociation width on this plane is very small. The energies of the other faults are not known. The diffusive motion of the whole dislocation should have the kinetics of the Cottrell effect if the dissociation width depends on the dislocation velocity in a similar way as the width of the Cottrell cloud. As described in a paper on FeAl [24], such a model explains all features observed, the occurrence of a flow stress anomaly, the inverse dependence of the strain rate sensitivity on the strain rate or stress as well as the properties of the dislocations, their straight oriented shape and their dynamic behaviour with either unstable or viscous motion.

In $MoSi_2$, a flow stress anomaly occurs also on slip systems different from {110} 1/2⟨111⟩, in particular also on the system {011} ⟨100⟩ [5]. For this system, the dependence of the strain rate sensitivity on the deformation parameters and the dislocation behaviour have not been studied in detail so far. It was therefore the aim of the present paper to deform $MoSi_2$ single crystals along [110] where the {011} ⟨100⟩ slip system is activated, including stress relaxation tests to reveal the dependence of the strain rate sensitivity on the strain rate. In addition, the dislocation structures of the deformed specimens were studied in a high-voltage electron microscope (HVEM) and it was tried to perform *in situ* straining experiments in the same instrument to observe the dynamic dislocation behaviour.

2 Experimental

Specimens for compression tests were cut from $MoSi_2$ single crystals by spark erosion with a [110] compression axis and $(1\bar{1}0)$ and (001) side faces. The faces were carefully ground and polished. The specimens were deformed in a digitally controlled single screw testing machine at a basic strain rate of 10^{-5} s^{-1}. Usually, the specimens were deformed at a single temperature, but at some samples the temperature was changed during the experiment in order to obtain data from different temperatures and to determine the activation energy. The strain rate sensitivity of the flow stress $r = \mathrm{d}\sigma/\mathrm{d}\ln\dot{\varepsilon}$ was measured from stress relaxation tests. Here, σ is the flow stress and $\dot{\varepsilon}$ the plastic strain rate. The data were plotted as the logarithm of the relaxation rate $-\dot{\sigma}$ versus the flow stress. The relaxation rate is proportional to the instantaneous strain rate. In these plots, the strain rate sensitivity is given by the reciprocal slope of the curves, $r = \mathrm{d}\sigma/\mathrm{d}\ln(-\dot{\sigma})$. The r values were determined at the beginning of the relaxation curves, thus corresponding to the strain rate from which the relaxation tests were started, and at the end of the relaxation curves, i.e., at a considerably lower strain rate.

Specimens for transmission electron microscopy were cut from the deformed samples parallel to the (110) cross section plane or to the (001) or $(1\bar{1}0)$ side faces. They were carefully polished and dimpled and finally thinned by argon ion milling. The dislocation structures were studied in an HVEM at an acceleration voltage of 1000 kV using high-order bright field diffraction contrast.

It was tried to perform *in situ* straining experiments inside the HVEM. Micro-tensile specimens were prepared by similar methods from samples predeformed in compression in order to make the specimens less brittle. The micro-tensile specimens with a (001) foil plane were loaded in tension along [110] in a special double-tilting high-temperature straining stage [25].

3 Results

3.1 Macroscopic deformation data

Figure 1 shows a typical stress-strain curve with several stress relaxation tests R_1 to R_5 and a temperature change. σ is the engineering stress and ε_t the total engineering strain. The stress-strain curves are smooth

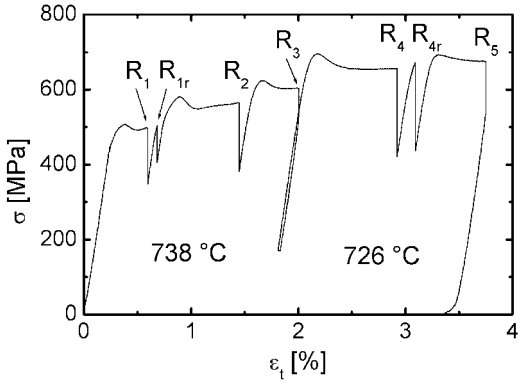

Fig. 1 Stress-strain curve of a deformation experiment at 738 °C and 726 °C. Strain rate 10^{-5} s^{-1}. R_n stress relaxation tests and R_{nr} repeated relaxation tests.

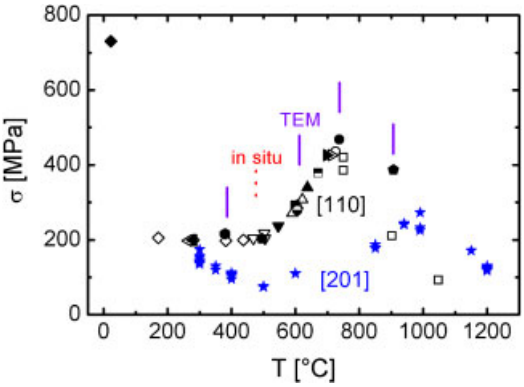

Fig. 2 (online colour at: www.pss-a.com) Temperature dependence of the yield stress. Full symbols: data from first loading of a specimen. Open symbols: data taken after temperature changes corrected for work-hardening. Fivefold (blue) stars: data from [21] for deformation along [201] for comparison.

at all temperatures except at 907 °C where jerky flow occurs. Yield point effects are observed below about 300 °C and above about 700 °C at the beginning of the curves and after relaxation tests and temperature changes. The work-hardening rate is high, about 25 GPa at 200 °C. It increases up to about 35 Pa at 500 °C and falls down to small values above 700 °C.

The temperature dependence of the yield stress is presented in Fig. 2. The lower yield point is taken for the yield stress at curves with a yield drop effect at the beginning. Otherwise, the work-hardening range is extrapolated linearly onto the elastic line. Full symbols represent data measured during first loading. The data plotted as open symbols were taken after temperature changes, with the stress contribution due to work-hardening being subtracted. The temperature dependence shows three main ranges. In the low-temperature range up to about 450 °C, the yield stress decreases strongly in the normal way. Between about 450 °C and 730 °C, a flow stress anomaly occurs with a strongly increasing flow stress. Above 730 °C, the usual high-temperature decrease of the flow stress is observed. For comparison, Fig. 2 exhibits also the temperature dependence of the yield stress for deformation along the [201] direction taken from [18, 21]. Both, the minimum between the low-temperature and the anomaly ranges and the flow stress peak are shifted to higher temperatures. Besides, the peak stress is much lower.

As described in Section 2, the strain rate sensitivity r of the flow stress was measured by stress relaxation tests. Figure 3 shows some stress relaxation curves with the logarithm of the relaxation rates plotted

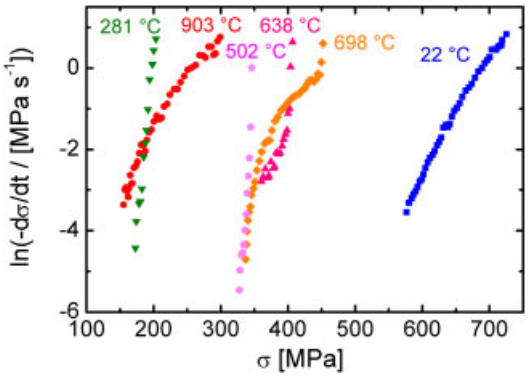

Fig. 3 (online colour at: www.pss-a.com) Stress relaxation curves at different temperatures.

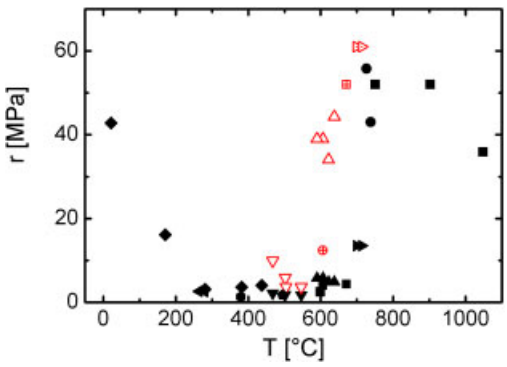

Fig. 4 (online colour at: www.pss-a.com) Temperature dependence of the strain rate sensitivity. Full symbols: data from the beginning of the relaxation tests belonging to the strain rate prior to the tests. Open symbols: for relaxation curves with inverse curvature, data belonging to a lower strain rate of about 10^{-7} s^{-1} (corresponding to about $\ln(-\dot{\sigma}/[\mathrm{MPa\ s^{-1}}]) = -3$).

as a function of the stress. As described in Section 2, the strain rate sensitivity r is given by the reciprocal slope of these curves. At room temperature, the curve shows the normal bending towards the stress axis. Such curves are obtained for most obstacle mechanisms controlling the strain rate sensitivity. At increasing temperature (281 °C), the curves with normal curvature become very steep, corresponding to low values of r. At the beginning of the anomaly range at 502 °C, the curve is still very steep but it starts to show an inverse curvature with the strain rate sensitivity increasing at decreasing strain rate or stress. At higher temperatures in the anomaly range (638 °C, 698 °C), the curves are steep at the beginning but show then clearly an inverse curvature. Only at low strain rates, the curves bend back to the normal curvature as demonstrated for 698 °C. At high temperatures, the curves become their normal curvature again. The strain rate sensitivity belonging to the strain rate before the tests is measured from the reciprocal slope at the beginning of the curves. In Fig. 4, these values are plotted by full symbols as a function of the temperature. The strain rate sensitivity decreases strongly in the low-temperature range of the flow stress. It is very small in the anomaly range and increases sharply at the transition to the normal high-temperature range. To summarize the inverse behaviour of the relaxation curves in the anomaly range, r values were measured at a lower strain rate (about 10^{-7} s^{-1} corresponding to about ln $(-\dot{\sigma}/[\text{MPa s}^{-1}]) = -3$). These data are plotted in Fig. 4 as open (red) symbols. As indicated by the inverse curvature of the relaxation curves, these values are greater than those corresponding to the initial higher strain rate. The low-strain rate data with normal behaviour in the ranges of the normal temperature dependence of the flow stress are not included in Fig. 4.

In some cases, so-called repeated relaxation tests R_{nr} were performed, i.e., relaxation tests started during reloading after a first relaxation test before steady state deformation was achieved again, like the tests R_{1r} and R_{4r} in Fig. 1. At their beginning, these repeated relaxation curves show lower relaxation rates than the original relaxation curves indicating changes of the microstructure during the initial relaxations. These effects are accompanied with the yield drop effects during full reloading as demonstrated in Fig. 1, too.

As described in Section 4.2, stress relaxation curves can also yield information on the so-called effective stress. In Fig. 3, relaxation curves with normal curvature are bent towards the stress axis, i.e., they converge against a certain stress value. In this case, the difference between the starting stress of the relaxation test and the final stress may be called the relaxing stress $\Delta\sigma_{rel}$. Values of $\Delta\sigma_{rel}$ cannot be obtained from short stress relaxation curves as that for room temperature or from curves with inverse curvature in the anomaly range as that for 638 °C. In the high-temperature range, the internal stress can also relax owing to recovery. The few values of $\Delta\sigma_{rel}$ obtained are plotted in Fig. 5 as a function of temperature.

In the ranges of the normal decrease of the flow stress, the activation enthalpy can be determined by

$$\Delta H = -kT^2 \frac{\Delta\sigma/\Delta T}{r}. \tag{3}$$

k is Boltzmann's constant and T the absolute temperature. The values correspond to the actual conditions of stress and temperature. As shown in [26] for the double-kink mechanism, the activation energy at zero

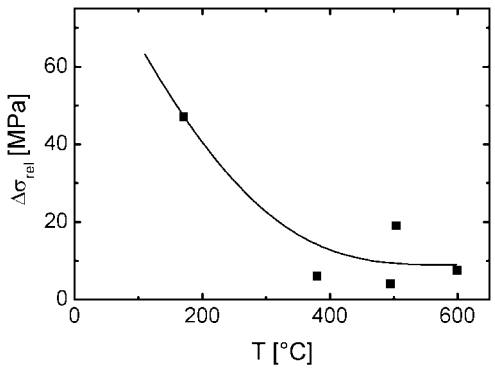

Fig. 5 Temperature dependence of the relaxing stress $\Delta\sigma_{rel}$.

stress, which characterizes the dislocation mechanism, may be about 10 or 20 % higher. From the few temperature change tests performed, the temperature sensitivity of the flow stress $\Delta\sigma/\Delta T$ at room temperature is about −2 MPa K^{-1} and −1.2 MPa K^{-1} in the high-temperature range. Using characteristic r values from Fig. 4 yields activation enthalpies of about 0.4 eV at room temperature and 2.5 eV at 800 °C.

3.2 Transmission electron microscopy of deformed specimens

The temperatures at which the dislocation structures were analysed are marked in Fig. 2 by the (violet) vertical lines. In a number of cases, the Burgers vectors of the dislocations were determined by the $\boldsymbol{g} \cdot \boldsymbol{b} = 0$ contrast extinction rule. An example is presented in Fig. 6 with a dislocation structure near a precipitate. The precipitates are of a very low density. The dislocations were generated by deformation at 380 °C. The specimen was cut parallel to a $(1\bar{1}0)$ side face. In Fig. 6a with $\boldsymbol{g} = (110)$, all dislocations are visible. A family of dislocations marked A is invisible in Fig. 6b with $\boldsymbol{g} = (\bar{1}03)$. Another family marked B is extinguished in Fig. 6c with $\boldsymbol{g} = (0\bar{1}3)$. All dislocations except some small dislocation loops are extinct in Fig. 6d with $\boldsymbol{g} = (002)$. Thus, the dislocations A have Burgers vectors parallel to [010] and those labelled B parallel to [100]. These Burgers vectors dominate in all specimens studied.

Figure 7 presents the dislocation structure from a specimen cut parallel to the (001) side face from the same deformation experiment. In this projection, all four {101} slip planes are inclined to the foil plane (in contrast to Figs. 6b and d, where two of the four slip planes are imaged edge-on). It is obvious that the dislocations are curved at this temperature at the end of the normal low-temperature range of the flow stress. The dislocation density was measured in a larger area of the same specimen by counting the number of intersections N of the dislocations with straight lines of different orientations with the total length L. The dislocation density was calculated by $\rho = 2N/(Lt)$ [27]. t is the thickness of the foil. It was estimated to be about 0.7 µm from another micrograph from the length of inclined dislocations. For the conditions of Fig. 7, i.e., a deformation at 380 °C by 0.4% plastic strain, ρ amounts to about 2.8×10^{13} m^{-2}.

The dislocation structures in the lower part of the anomaly range are documented in Figs. 8 and 9 of a specimen deformed at 606 °C. The foil is cut parallel to the (001) side face of the compression sample. In Fig. 8, the specimen is imaged near the $[\bar{1}\bar{1}1]$ pole with $\boldsymbol{g} = (1\bar{1}0)$ so that all dislocations with ⟨100⟩ Burgers vectors are visible. Many dislocations are straight and oriented parallel to the traces of the (101) and (011) planes, which are imaged edge-on at the projection of the figure. Thus, it may be assumed that these dislocations are arranged on these slip planes. Figure 9 presents a specimen area close to that of Fig. 8 imaged with different $\boldsymbol{g}$ vectors near the [001] pole. In Fig. 9a with $\boldsymbol{g} = (1\bar{1}0)$, all dislocations are

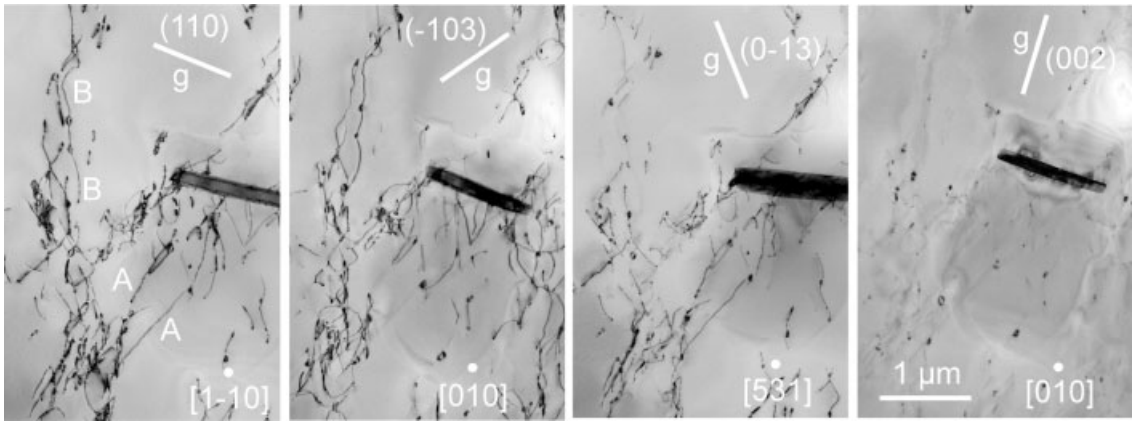

Fig. 6 Microstructure after deformation along ⟨110⟩ at 380 °C by 0.4% to final stress of 400 MPa imaged with different $\boldsymbol{g}$ vectors at different poles. The poles are indicated by the indexing at the white dot. Foil plane parallel to the $(1\bar{1}0)$ side face of the compression specimen.

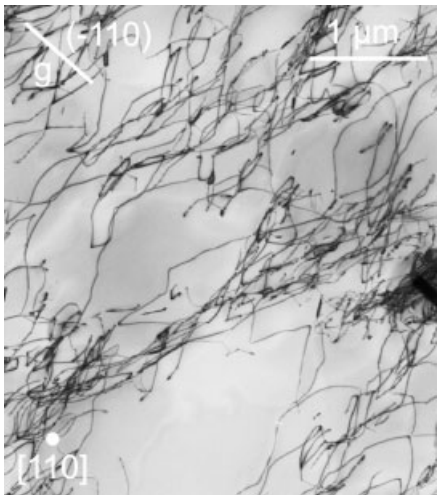

Fig. 7 Dislocation structure of the same deformation experiment as in Fig. 6. Foil plane parallel to (110) cross section plane.

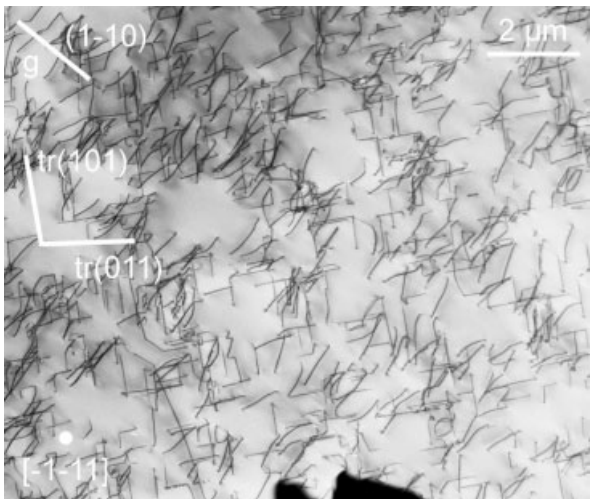

Fig. 8 Dislocation structure after deformation along ⟨110⟩ at 606 °C by 0.2% to final stress of 350 MPa. Foil plane parallel to (001) side face of compression specimen. The straight lines marked tr indicate the directions of the traces of the indicated planes imaged edge-on.

visible. One set of dislocations is extinguished in Fig. 9b with $\boldsymbol{g}$ = (020) and another one in Fig. 9c with $\boldsymbol{g}$ = (200). Accordingly, the dislocations have again the ⟨100⟩ Burgers vectors. Dislocations with Burgers vectors with a c component cannot be extinguished with these $\boldsymbol{g}$ vectors. In the projection of Fig. 9, most dislocations are also straight and oriented parallel to the $[1\bar{1}0]$ direction indicated by the $\boldsymbol{g}$ vector or to the perpendicular [110] direction. Thus, these dislocation lines are oriented along ⟨111⟩ directions. Because of their large edge component, they show relatively strong residual contrast at the extinctions with

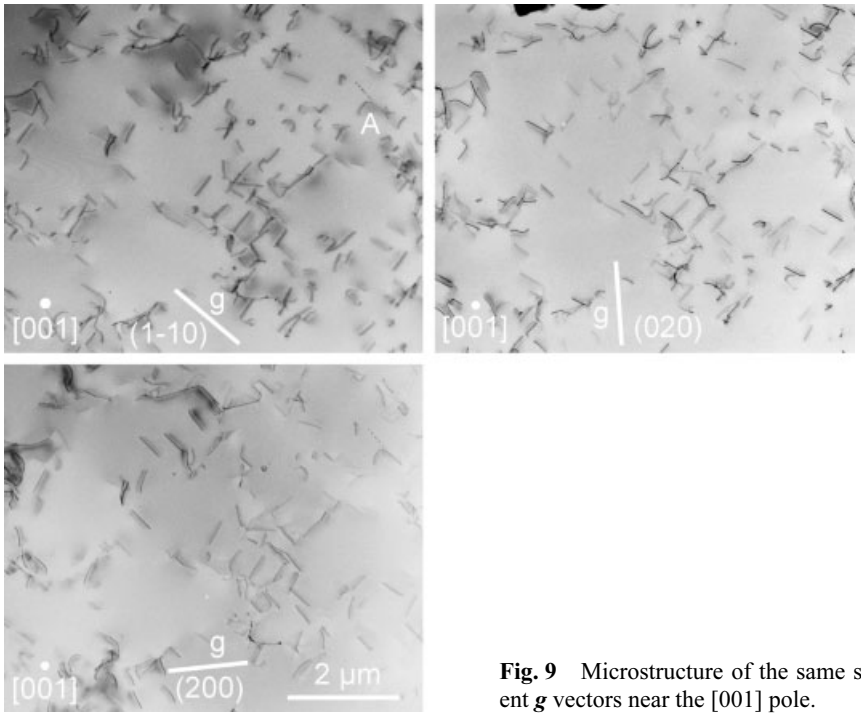

Fig. 9 Microstructure of the same specimen as Fig. 8 at different $\boldsymbol{g}$ vectors near the [001] pole.

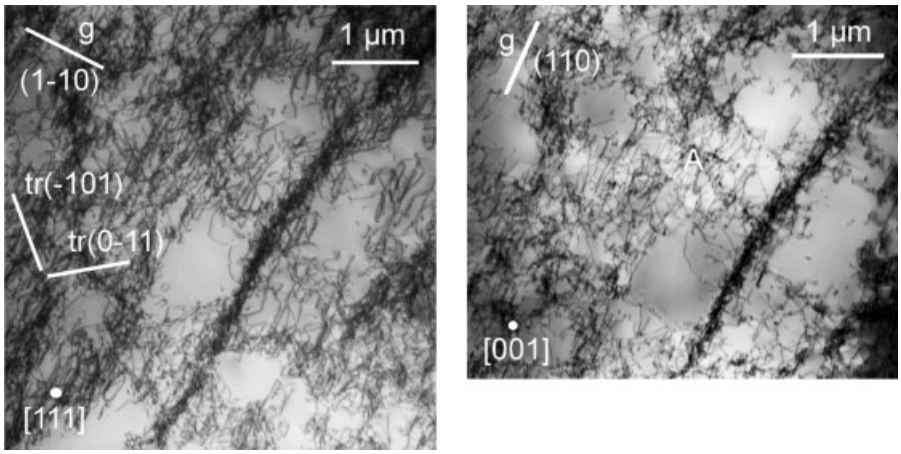

Fig. 10 Microstructure after deformation along ⟨110⟩ at 638/622/606/590 °C by 1.5% to final stress of 750 MPa at different poles and ***g*** vectors.

$\boldsymbol{g} \cdot \boldsymbol{b} = 0$ in Figs. 9b and c. In Fig. 8, the $[\bar{1}\,\bar{1}\,1]$ zone axis is always one of the ⟨111⟩ directions of the dislocations on the (101) and (011) planes imaged edge-on. Dislocations with other orientations are also imaged along the traces of these planes. Dislocations along the remaining ⟨111⟩ direction on the {101} planes which are not imaged edge-on are visible in diagonal direction between the former ones.

Figure 10 exhibits the dislocation structure of a specimen deformed at different temperatures around 615 °C, i.e., at similar temperatures as the specimen of Figs. 8 and 9, up to a considerably higher strain and stress. Near the [111] pole in Fig. 10a, many dislocations appear straight since they extend on the $(\bar{1}01)$ and $(0\bar{1}1)$ planes imaged edge-on. In Fig. 10b, a similar area is shown near the [001] pole. One family of dislocations marked A is approximately parallel to the [110] direction. These dislocations may be arranged again parallel to a ⟨111⟩ direction. In general, however, the dislocation structure is far less regular than that at the smaller strain. The dislocations form now a cell structure with bundles which appear also parallel to [110]. The bundles may form by the interaction between dislocations on the two {101} planes mentioned above which intersect along the [111] direction. The projection appears along [110].

The dislocation structures formed at a small strain at a higher temperature within the anomaly range (672 °C) are displayed in Figs. 11 and 12. Figure 11 is a stereo pair taken near the $[1\bar{1}0]$ pole. The compression axis is parallel to the (110) ***g*** vector. All four {101} slip planes are inclined to the foil plane at equal angles. The images show that the dislocations have angular shapes with segments appearing in the projections of the ⟨111⟩ directions. Figure 12 presents the same structure at the $[3\bar{3}\,\bar{1}]$ and [100] poles. In Figs. 12a and b, the two {301} reflections extinguish one set of dislocations each. In Fig. 12c taken with

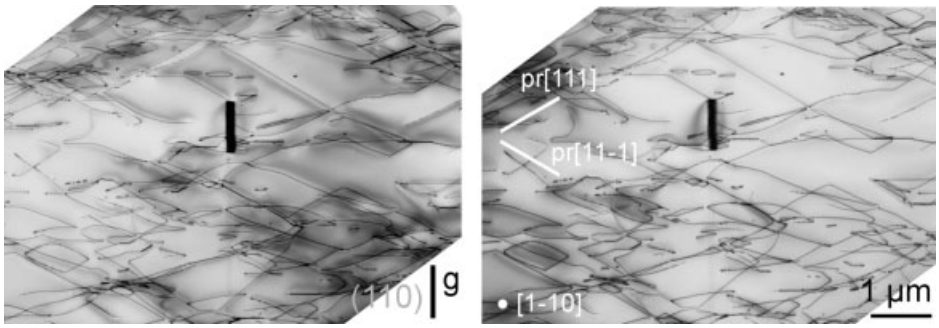

Fig. 11 Stereo pair of dislocation structure after deformation at 672 °C by 0.25% to a final stress of 450 MPa. The straight lines marked pr indicate the directions of the projections of the indicated orientations.

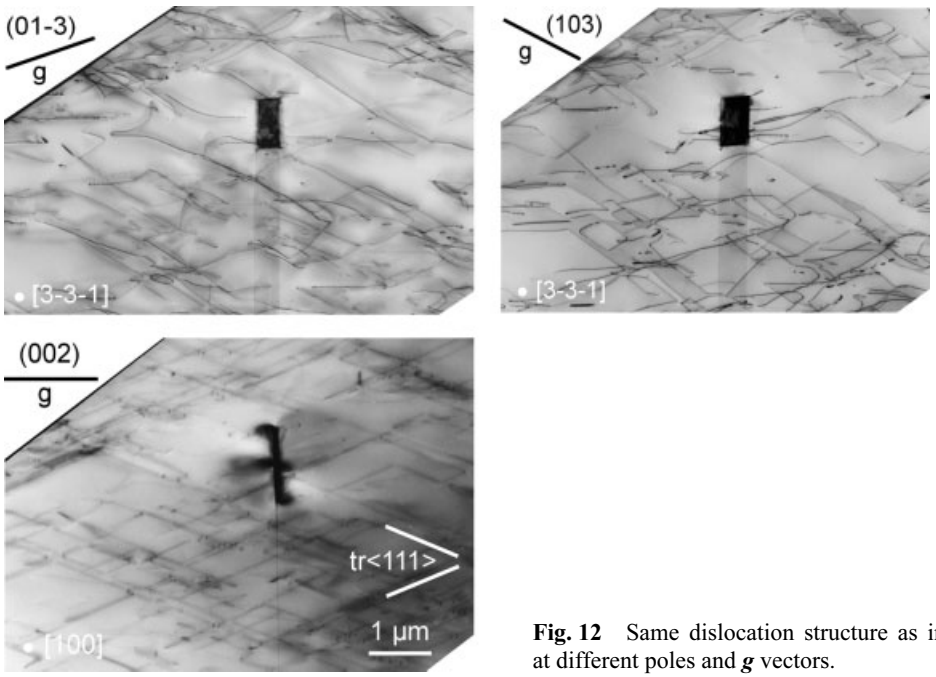

Fig. 12 Same dislocation structure as in Fig. 11 at different poles and ***g*** vectors.

the (002) reflection, all dislocations are extinguished, i.e., they appear only in a relatively strong residual contrast. Thus, the Burgers vectors are again parallel to [100] and [010]. In this projection, practically all dislocations are parallel to the projections of the four ⟨111⟩ directions. It may therefore be concluded that in the range of the flow stress anomaly, the dislocations with ⟨100⟩ Burgers vectors show strong preference orientations along ⟨111⟩.

In the high-temperature range, the dislocations are not strictly oriented anymore as demonstrated in Fig. 13, taken at the peak temperature. Of the four {101} slip planes, only the (011) planes are oriented edge on in this figure. No dislocations are imaged parallel to the traces of these planes. All dislocations are arranged on planes inclined to the viewing direction. Now, the dislocations bow smoothly out between cusps. There are many small loops which may have formed from the dislocation debris at the high temperature. In many cases, loops are situated at the cusps in the bowing dislocations, i.e., they act as obstacles.

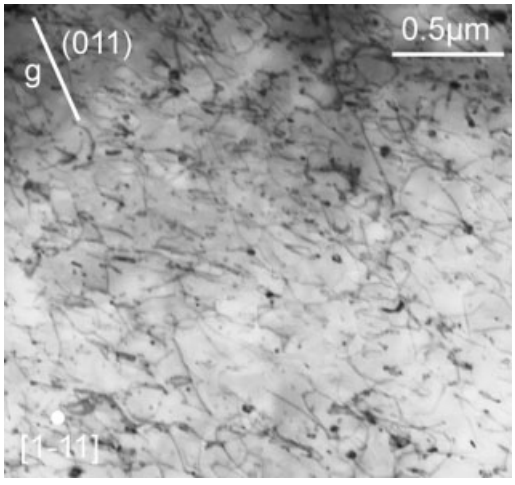

Fig. 13 Microstructure after deformation along ⟨110⟩ at 738/726 °C by 3.5% to a final stress of 680 MPa. Stress-strain curve in Fig. 1.

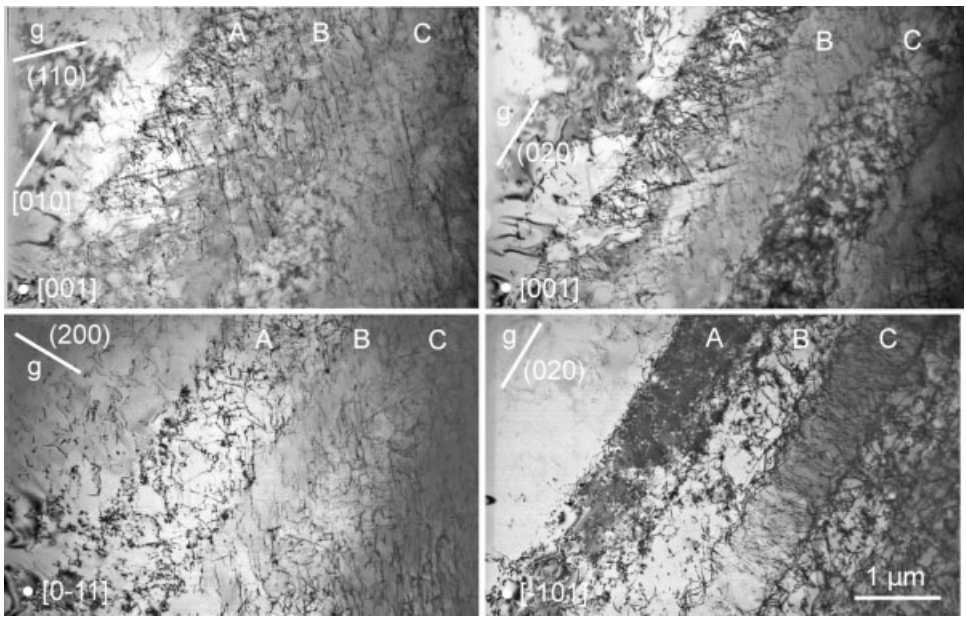

Fig. 14 Microstructure of the same specimen as in Fig. 13 at different poles and ***g*** vectors.

Figure 14 presents a specimen area with a higher dislocation density. Different slip systems have dominated in different specimen areas resulting in a band structure. Three bands are indicated by letters A to C. The borders between the bands run in the [010] direction. In the bands A and B, the projections of many dislocations run in the two ⟨110⟩ directions with [110] dominating in A and $[\bar{1}10]$ in B. These dislocations are visible both with the (110) and (020) ***g*** vectors in Figs. 14a and b but they are extinguished with ***g*** = (200) in Fig. 14c. Thus, their Burgers vector should be parallel to [010]. The borders between the bands with an increased dislocation density may have formed by the interaction between dislocations on (101) and $(\bar{1}01)$ planes which contain both the [010] Burgers vector and which intersect along this direction.

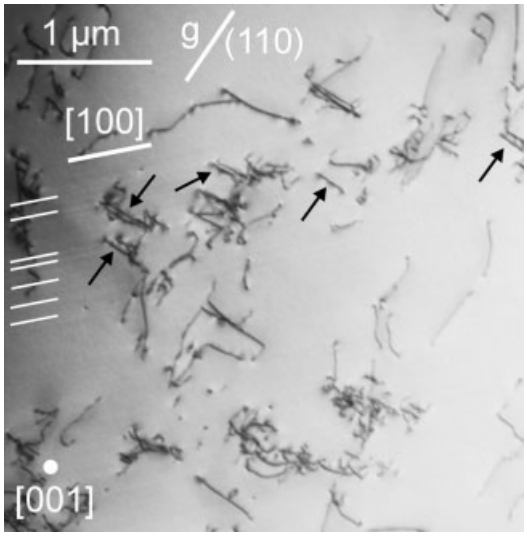

Fig. 15 Dislocations during *in situ* straining in an HVEM at 475 °C along ⟨110⟩ of a specimen predeformed at 606 °C.

3.3 *In situ* straining experiments

The micro-tensile specimens for the *in situ* straining experiments were cut from predeformed samples in order to reduce the brittleness. The predeformation was carried out at 495 °C at the minimum of the flow stress, at 606 °C at the beginning of the anomaly range and at 907 °C in the high-temperature range. *In situ* straining in the HVEM was tried at about 475 °C, 610 °C, 835 °C, and 970 °C. All experiments failed by brittle fracture without any sign of plastic deformation except the test at 475 °C near the flow stress minimum. Figure 15 presents the microstructure obtained. Most dislocations originate from the predeformation. Dislocations having moved during the *in situ* loading have produced slip traces, which are visible as weak bright lines. Some of them are labelled by short white lines near the left edge of the figure. At the [001] pole, the slip traces run in [100] directions, i.e., they belong to the (011) and $(0\bar{1}1)$ slip planes. Some of the dislocations which had moved are marked by black arrows. These dislocations are straight. Their projections follow the $[\bar{1}10]$ direction. Thus, the dislocation lines should be oriented again along ⟨111⟩ directions. Accordingly, this single successful *in situ* experiment confirms the result of the *post mortem* studies in Section 3.2 that the active dislocations are straight and oriented along ⟨111⟩ at intermediate temperatures.

4 Discussion

4.1 Elastic properties of dislocations

As a basis for the considerations below, the elastic properties of dislocations, i.e., the line energy and line tension as well as the shape of dislocations are calculated in the framework of elasticity theory in anisotropic elastic media. Using elastic constants from [28], line energies were determined before for dislocations on {110} planes with several Burgers vectors [29] but not for the present {011}⟨100⟩ slip system. In this study, the data were calculated using a PC programme written by D. Baither [30] with elastic constants for room temperature from [31] (in units of GPa: $c_{11} = 404$, $c_{12} = 115$, $c_{13} = 88$, $c_{33} = 505$, $c_{44} = 203$, $c_{66} = 195$), which are similar to those in [28]. The K values, which represent the shear moduli on specific slip systems, decrease with increasing temperature by about 0.026 GPa K^{-1}.

The equilibrium shapes of dislocations bowing out under load are plotted in Fig. 16. In addition to the present {011} ⟨100⟩ slip system also the $\{\bar{1}10\}$ ⟨111⟩ system is shown. The Burgers vectors are always parallel to the *x*-axis. Both dislocation shapes are smooth and resemble the elliptical shape of isotropic elasticity. For the {011} ⟨100⟩ slip system, the loop is even almost circular. In the representation of Fig. 16, the half axes parallel to the *x* and *y* axes correspond to the prelogarithmic energy factors E_s and E_e of screw and edge dislocations in units of 10^{-9} N. These values are 1.621 and 1.671 for {011} ⟨100⟩ and 3.133 and 3.796 for $\{\bar{1}10\}$ 1/2 ⟨111⟩. Thus, the latter are about twice as large as the former ones because of the larger Burgers vector.

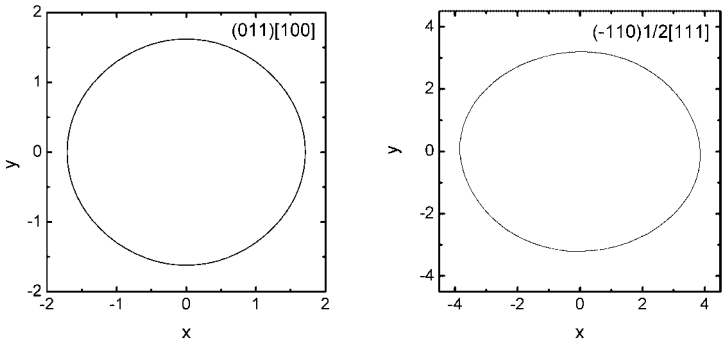

Fig. 16 Equilibrium shape of dislocations bowing out under load, calculated by the PC programme in [30]. The Burgers vectors are parallel to the *x*-axis. a) Dislocation with Burgers vector [100] on (011) plane. b) Dislocation with Burgers vector 1/2 [111] on $(\bar{1}10)$ plane.

4.2 The athermal stress component

According to [32], the total (shear) flow stress τ can be split into an athermal component τ_i and a thermal component τ^*,

$$\tau = \tau_i + \tau^* . \tag{4}$$

The first one is also called the internal stress and the second one the effective stress. Assuming a homogeneous distribution of dislocations, the athermal component of the flow stress can be estimated by the formula for Taylor hardening [33]

$$\tau_i = \alpha \mu b \sqrt{\rho}, \tag{5}$$

where α is a numerical factor between 0.1 and 1, μ, the shear modulus, b, the absolute value of the Burgers vector and ρ the dislocation density. The numerical constant is set to the frequently used value of $\alpha = 0.5$. The shear modulus μ is replaced by the ansiotropic K value for the screw dislocation, $K_s = 4\pi E_s/b^2 = 198.4$ GPa. With the dislocation density $\rho = 2.8 \times 10^{13}$ m^{-2} from Section 3.2 for deformation at 380 °C, the athermal stress component becomes $\tau_i \cong 170$ MPa. As shown in the caption of Fig. 6, the engineering flow stress σ at the end of this experiment is 400 MPa. The engineering stress is related to the shear stress by $\tau = m_s \sigma$, where m_s is the orientation factor. For loading along ⟨110⟩, the orientation factor of the {011} ⟨100⟩ system is $m_s = 0.46$, resulting in a macroscopic (shear) flow stress of $\tau = 184$ MPa. Thus, the estimated athermal stress component τ_i is slightly lower than the total flow stress τ. This estimation shows that the athermal stress component represents most probably a large part of the total flow stress and cannot be neglected, especially in the range of the flow stress minimum. The large athermal stress contribution is in agreement with high work-hardening rates between 200 °C and 700 °C, in particular in the anomaly range. Unfortunately, not enough micrographs were obtained in this work to study the temperature dependence of the athermal stress component on the temperature at a fixed small plastic strain.

However, it may be assumed that the effective stress can completely relax after long times during a stress relaxation experiment. In this sense, the relaxing stresses plotted in Fig. 5 may be considered lower limits of the effective stress. Converted to shear stresses, τ^* may amount to only about 5 MPa between 400 °C and 600 °C and increases to about 22 MPa at 170 °C. This is in the order of magnitude of 10% of the total shear flow stress. Thus, in the low-temperature range, the athermal stress component is the dominating part of the flow stress.

4.3 The low-temperature range

As described in Section 3.1 and demonstrated in Fig. 2, $MoSi_2$ deformed along ⟨110⟩ shows a strong normal decrease of the flow stress between room temperature and about 300 °C. It is suggested here that this behaviour results from the action of the Peierls mechanism, in addition to the decrease of the athermal stress component. In the present study, no micrographs are available in the low-temperature range but in [5] the dislocations tend to align along ⟨111⟩ at room temperature.

The detailed theory of the Peierls mechanism of [34] yields the dependence of the Gibbs free energy of activation on the effective stress τ^* for the double-kink mechanism as

$$\Delta G(\tau^*) = 2G_k \left[1 - \frac{\pi \tau^*}{8\tau_p} \left(\ln \frac{16\tau_p}{\pi \tau^*} + 1 \right) \right], \tag{6}$$

with G_k being the energy of a single kink and τ_p the Peierls stress at $T = 0$ K. From this potential, there follows the activation volume

$$V(\tau^*) = -\frac{\partial \Delta G}{\partial \tau^*} = \frac{\pi G_k}{4\tau_p} \ln \frac{16\tau_p}{\pi \tau^*} . \tag{7}$$

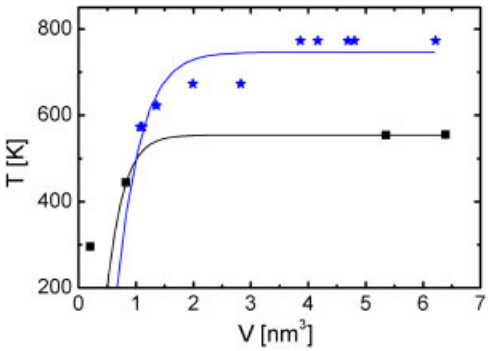

Fig. 17 Plot of temperature T versus activation volume V for deformations along ⟨110⟩ with data below 300 °C (black squares) and deformation along ⟨201⟩ at and below 500 °C (blue stars). Theoretical curves with Eq. (9) and the data in Section 4.3.

As discussed in Section 4.2, the athermal stress component is large but not well known so that an analysis of V vs. τ^* is not possible. Therefore, Eqs. (6) and (7) together with the Arrhenius equation

$$\dot{\varepsilon} = \dot{\varepsilon}_0 \exp(-\Delta G/kT) \tag{8}$$

were solved for T. Here, $\dot{\varepsilon}$ is the strain rate and $\dot{\varepsilon}_0$ a pre-exponential factor. The latter is supposed to be constant. The result is

$$T = T_0 [1 - 2\exp(-\chi V)(\chi V + 1)] \tag{9}$$

with

$$T_0 \equiv \frac{2G_k}{k \ln(\dot{\varepsilon}_0/\dot{\varepsilon})} \quad \text{and} \quad \chi \equiv \frac{4\tau_p}{\pi G_k} .$$

Figure 17 presents the respective plot for temperatures below 300 °C where the Peierls mechanism is supposed to operate. In the respective regression curve, the room temperature point is not considered. If it is included, the curve does not meet the two data points at the high-temperature end. The regression analysis yielded the values T_0 = 554 K and χ = 4.71 nm^{-3}. With $\ln(\dot{\varepsilon}_0/\dot{\varepsilon}) = 20$, it follows that G_k = 0.48 eV and τ_p = 282 MPa. The kink energy assumes a reasonable value. According to Eqs. (6) and (8), the theoretical value of the activation energy is 0.5 eV, which is consistent with the activation enthalpy of 0.4 eV determined from the temperature change test (Section 3.1) while the Peierls stress at 0 K is quite small.

According to the elastic theory of the Peierls mechanism (as described, e.g., in [35]), the Peierls stress is related to the Peierls energy

$$U_p = \frac{\tau_p w b}{\pi} \tag{10}$$

and this in turn to the kink energy

$$G_k = \frac{2w}{\pi}\sqrt{2U_p \Gamma} . \tag{11}$$

Here, w is the width of the Peierls valleys, which is set $w = b$, and Γ is the line tension. For the present screw dislocation, the line tension is almost equal to the line energy, so that $\Gamma \cong \ln(R/r_0)\, E_s = 6.37\, E_s$, if $1/\sqrt{\rho}$ is set for the outer cut-off radius R of the dislocations with $\rho = 2.8 \times 10^{13}$ m^{-2} from Section 3.2 and $r_0 = b$ for the inner one. With these data and the value of the Peierls stress above, the kink energy would be G_k = 0.55 eV. This value is close to that from the regression analysis of the activation volume. That means that the parameters of the Peierls mechanism, G_k and τ_p, determined above are consistent within the framework of the elastic theory of this mechanism.

The low value of τ_p = 282 MPa with respect to the flow stress at room temperature, τ = 336 MPa, emphasizes the large contribution of the long-range internal stress to the total flow stress, as discussed in

the previous section. If the dislocation multiplication and consequently the dislocation density are triggered by the effective stress due to the Peierls mechanism, a Cottrell–Stokes like behaviour may result, i.e., the increasing effective stress from the Peierls mechanism with decreasing temperature causes also an increasing athermal stress component, which may even be greater than the thermal one.

The present data may be compared with those for the ⟨201⟩ orientation where the $\{\bar{1}10\}\langle 111\rangle$ slip system is activated. As shown in Fig. 2, the flow stress minimum, which marks the end of the range of the Peierls mechanism, is at about 500 °C with respect to about 300 °C for the ⟨110⟩ orientation. Similarly, the minimum of the strain rate sensitivity is also shifted to higher temperatures [19, 21]. The T vs. V plot for the strain rate cycling data of the ⟨201⟩ orientation is included in Fig. 17. It shows the higher limiting temperature of T_0 = 746 K and a coefficient χ = 3.25 nm^{-3}. This yields G_k = 0.64 eV and τ_p = 263 MPa. The higher value of G_k can be understood from the larger absolute value of the Burgers vector (0.3204 nm for $b = \langle 100\rangle$ and 0.4531 nm for $b = 1/2\langle 111\rangle$) in Eqs. (10) and (11), resulting also in a higher line tension (see the line energy data in Section 4.1). Thus, the Peierls mechanism can interpret the low-temperature decrease of the flow stress and its different temperature ranges for the two orientations. Flow stress data for the $\{\bar{1}10\}\langle 111\rangle$ slip system below 300 °C are not available.

4.4 The anomaly range

In this paper, it is tried to explain the occurrence of the flow stress anomaly for the $\{011\}\langle 100\rangle$ slip system by a similar mechanism as that suggested already for the $\{110\}\ 1/2\langle 111\rangle$ slip system in [21]. It is based on the model in [22] for the motion of dislocations with ⟨110⟩ Burgers vectors in NiAl. For the $\{110\}\ 1/2\langle 111\rangle$ slip system in $MoSi_2$, it is assumed that the dislocations dissociate by glide according to Eq. (2). In most of the literature, a dissociation of dislocations with $1/2\langle 111\rangle$ Burgers vectors according to Eq. (1) is stated. The results in [5] confirm this reaction for screw dislocations but show a dissociation outside the {110} plane for dislocations with an edge component. The reaction in Eq. (2) is favoured by a small gain in elastic energy. Besides, the dislocations with $1/2\langle 111\rangle$ Burgers vectors seem generally not to be very stable [36]. The resulting dislocation core is not planar. The total dislocation can move on its glide plane only by a combination of glide and so-called conservative climb, i.e. the emission of vacancies by one partial dislocation and the absorption of these vacancies by another one. The original model in [22] has to be extended by assuming that the dissociation width depends on the dislocation velocity [21]. This may lead to a dynamic behaviour which can be described by the kinetics of the Cottrell effect [15].

The following experimental observations favour the proposed model.

– In the anomaly range, dislocations tend to orient along specific crystallographic directions. For the dislocations with ⟨100⟩ Burgers vectors on {011} planes, these are the ⟨111⟩ directions (Figs. 8 to 12). The crystallographic orientation is not a consequence of an anisotropy of the line tension. As shown in Fig. 16, the elastic equilibrium shape is smoothly curved for both slip systems. The dislocations are curved and not oriented in the range of the flow stress minimum below the anomaly range (Fig. 7) as well as at high temperatures above the anomaly range (Figs. 13 and 14).

– The strain rate sensitivity is small in the anomaly range (Fig. 4) and it shows an inverse dependence on the strain rate, i.e., the strain rate sensitivity is higher for smaller strain rates or stresses (Figs. 3 and 4). This dynamic behaviour can be described by the kinetics of the Cottrell effect. It causes a contribution to the flow stress $\Delta\sigma_c$ which shows a maximum with increasing strain rate (or decreasing temperature). The slope in a plot of $\Delta\sigma_c$ vs. $\ln\dot{\varepsilon}$ corresponds to the strain rate sensitivity r. It is zero at the maximum, negative at higher strain rates and positive with the inverse strain rate dependence at lower ones.

Negative strain rate sensitivities cannot be observed by stress relaxation tests which were applied in the present study. They are usually connected with plastic instabilities. Instabilities have been observed in the anomaly range for deformation along ⟨201⟩ but not in the present work. The origin of serrated flow in a single experiment at 907 °C is obscure.

The model described above is based on the occurrence of dislocations with a non-planar core along specific orientations by glide dissociation on low-index planes. During the motion, the dislocation does not constrict as in other models but moves by a combination of glide and conservative climb within the dislocation core, which requires diffusion processes. The importance of diffusion processes in connection

with the flow stress anomaly was noted before not only in [16] but also in [37]. Since a detailed theory of the climb process with a changing distance between the source and sink dislocations does not exist, the theory of the Cottrell effect can be used as a first approximation. In both cases, point defects have to move in the forward direction of the dislocation. Such a model seems to be appropriate for a number of materials. It has been suggested previously for FeAl [24]. For the dislocations with ⟨100⟩ Burgers vectors oriented along ⟨111⟩ a dissociation reaction is suggested in [38]

$$[100]\,(0\bar{1}1) \rightarrow 1/6[301]\,(12\bar{3}) + 1/6[30\bar{1}]\,(1\bar{4}3)\,. \tag{12}$$

The three slip planes involved intersect along the [111] preference direction of the dislocations. The total dislocation forms an angle of 69.3 ° between the [100] Burgers vector and the [111] line direction. In anisotropic elasticity theory with the elastic constants mentioned in Section 4.1, the prelogarithmic energy factor is 1.52×10^{-9} N. The component dislocations form angles of 34.8 ° and 105.9 ° with the line direction and have energy factors of 7.05×10^{-10} and 7.38×10^{-10} N. Thus, the reaction is accompanied with an energy gain of about 5%. The component dislocations have different orientation factors for glide at the [110] compression axis. The total dislocation can only move on its $(0\bar{1}1)$ slip plane by a vacancy flux from one partial to the other.

Unfortunately, theoretical calculations of core configurations and respective planar faults are available only for dislocations with 1/2⟨331⟩ and 1/2⟨111⟩ Burgers vectors [23, 38, 39] but not for ⟨100⟩. Thus, both experimental and theoretical work is necessary to prove this reaction.

Since a theory of the conservative climb model with velocity and temperature depending dissociation width is not yet available, some estimations are made regarding the position and height of the flow stress maximum using the theory of the Cottrell effect as it is described in [35]. The temperature T_{max} of the flow stress maximum is given by

$$T_{max} = \frac{\dot{\varepsilon}\beta}{4\rho bkD}, \tag{13}$$

where ρ is again the dislocation density, D the diffusion coefficient of the diffusing species and β an interaction constant given by

$$\beta = \frac{\mu b}{3\pi}\frac{1+\nu}{1-\nu}\,v_{rel}. \tag{14}$$

μ is again the shear modulus, which, for the Cottrell effect, is replaced by the anisotropic K value of the edge dislocation K_e. With elastic constants for 650 °C, K_e = 187.2 GPa. ν is Poisson's ratio. It is replaced by $\nu = 1 - E_s/E_e$, with E_s and E_e being the prelogarithmic energy factors of screw and edge dislocations. In agreement with the almost circular equilibrium shape of the dislocations with ⟨100⟩ Burgers vectors (Fig. 16a), ν is very small: $\nu = 0.04$. By comparing Eqs. (14–47) and (14–42) of [35], it may be concluded that the relaxed volume of a vacancy v_{rel} should enter Eq. (14) if the diffusion takes place by the motion of vacancies. It is assumed here that v_{rel} equals about 30% of the atomic volume, i.e., $v_{rel} = 0.3\ a^2\ c/6$. a and c are the lattice constants. With these data, one obtains $\beta \cong 2.8 \times 10^{-29}$ N m^2. Then, it follows from Eq. (14) that the diffusion coefficient should be about $D \cong 5 \times 10^{-19}$ m^2 s^{-1} to obtain the flow stress maximum at a strain rate $\dot{\varepsilon} = 10^{-5}$ s^{-1} and a temperature of T_{max} = 1010 K (Fig. 2). Diffusion coefficients for both Mo and Si in $MoSi_2$ single crystals have been published in [40, 41]. According to these measurements, the diffusion coefficients are strongly anisotropic with higher diffusivities perpendicular to the c-axis than parallel to it. Besides, in the temperature range considered, only Si diffuses. Comparable diffusion coefficients for Mo are observed only above about 1500 K. This agrees with the result from a positron annihilation study that the thermal vacancies are situated on the Si sublattice [42]. The Si diffusion coefficients at 1010 K are about 10^{-16} m^2 s^{-1} for diffusion perpendicular to the c-axis and 3×10^{-18} m^2 s^{-1} for diffusion parallel to it. Thus, the experimental diffusion coefficients of Si are considerably higher than that required for diffusion in the dislocation core for the Cottrell effect. However, climb-controlled motion of the dislocation requires the diffusion of both constituents, i.e., Si and Mo, so that the slower species should determine the total rate. Mo bulk diffusion is far too slow so that the model requires strongly enhanced diffusion in the dislocation core.

The maximum value of the contribution of the Cottrell effect to the flow stress can be estimated as

$$\Delta\sigma_{c,\max} = \frac{17c\beta}{m_s b^4}\,, \tag{15}$$

where c is the concentration of the diffusing defect. The experimental value of $\Delta\sigma_{c,\max}$ is 280 MPa. The necessary concentration of the vacancies would then be $c = 3 \times 10^{-3}$. This value is relevant for the previous model [16], where the dislocations acquire a certain vacancy concentration to reach the minimum energy configuration. For the present dissociation model, the meaning of Eq. (15) is not quite clear.

The proposed mechanism should explain the different positions of the flow stress maximum for deformation along ⟨110⟩ and ⟨201⟩. For dislocations with 1/2⟨111⟩ Burgers vectors on {110} planes, the value K_e = 213.5 GPa to be inserted in Eq. (14) for the shear modulus at 650 °C is only slightly greater than the respective value for the {011} ⟨100⟩ slip system. The remarkably larger Burgers vector cancels if Eq. (14) is inserted into Eq. (13). However, an essential difference may arise from the anisotropy of the diffusion coefficient. In each case, the transport of matter has to occur in the direction of motion of the dislocation. For the dislocations with ⟨100⟩ Burgers vectors and ⟨111⟩ line directions, the transport occurs essentially perpendicular to the c-axis. This is the direction of a high diffusion coefficient. Alternatively, the direction of motion of dislocations with 1/2⟨111⟩ Burgers vectors aligned along ⟨110⟩ has a large component parallel to the c-axis. In this direction, the diffusion coefficients of both Si and Mo are considerably lower than perpendicular to it which, according to Eq. (13), results in a higher temperature $T_{\max}$ of the flow stress maximum as observed in Fig. 2. The maximum contribution to the flow stress $\Delta\sigma_{c,\max}$ in Eq. (15) is proportional to b^{-3}. This may lead to a smaller value of $\Delta\sigma_{c,\max}$ for deformation along ⟨201⟩ under otherwise similar conditions.

In addition to the mechanism causing the flow stress anomaly, there is certainly also a large athermal flow stress component due to long-range dislocation interactions. As described in Section 4.2, it dominates at the flow stress minimum between 300 °C and 500 °C and it may even increase in the anomaly range triggered by the increasing anomalous stress contribution.

The present model is a first attempt to interpret the straight oriented course of the dislocations and the inverse dependence of the strain rate sensitivity on the strain rate in the range of the flow stress anomaly for both main slip systems in $MoSi_2$. In the present form, it explains most experimental observations in a qualitative sense but it lacks direct experimental evidence as well as detailed theoretical modelling. However, it may guide future work.

4.5 The high-temperature range

Above the flow stress peak, the flow stress decreases in the normal way. For this range, this work presents data of very few experiments, only. Already at the flow stress peak, the dislocations do not show anymore the strictly oriented shape characteristic of the anomaly range (Fig. 13). In regions of a high dislocation density, a band structure occurs (Fig. 14), which points at long-range dislocation interactions. As in other materials, the flow stress may be controlled by recovery. Since the work-hardening is low, the high-temperature deformation can conveniently be treated in terms of an equation for steady state creep (see, e.g., [43])

$$\dot{\varepsilon}_{ss} = A\frac{\mu b}{kT}\left(\frac{\sigma}{\mu}\right)^m D_0 \exp\left(-\frac{\Delta H}{kT}\right), \tag{16}$$

where A is a dimensionless constant, m the stress exponent for creep, D_0 the pre-exponential factor and ΔH the activation enthalpy of the respective diffusion process. Depending on the particular creep model, stress exponents are expected between about 4 and 6. Stress exponents m can be determined from the strain rate sensitivity r according to

$$m = \frac{d\ln\dot{\varepsilon}}{d\ln\sigma} = \frac{\sigma}{r}\,. \tag{17}$$

From a single experiment in the high-temperature range, it follows that m decreases from about 7.5 at 750 °C down to 2.5 at 1050 °C. Thus, the experimental m values agree with the theoretical one in the middle of the high-temperature range. The activation enthalpy should correspond to the activation enthalpy for self diffusion. The experimental value is 2.5 eV at 800 °C (Section 3.1) and the diffusion enthalpies are 1.93 and 2.33 eV for diffusion of Si and about 5.4 and 6.2 eV for diffusion of Mo, perpendicular and parallel to the c-axis each. Accordingly, there is a similar situation as for the Cottrell effect interpretation of the anomaly range: the diffusion data required for the respective model are between the data for diffusion of Si and Mo. At present, a convincing interpretation of this fact cannot be given. For other intermetallic materials, there does not occur such a great difference between the diffusion data of the different constituents.

5 Conclusions

The following conclusions can be drawn.

– Plastic deformation of $MoSi_2$ single crystals along a ⟨110⟩ axis is carried by dislocations with ⟨100⟩ Burgers vectors moving on {011} planes. The temperature dependence of the flow stress shows three ranges as for the {110} 1/2⟨111⟩ slip system: a low-temperature range with a normally decreasing flow stress, an anomaly range with an increasing flow stress and a high-temperature range with a normally decreasing flow stress.

– The low-temperature behaviour can be interpreted by the action of the Peierls mechanism superimposed on a large athermal flow stress component.

– Based on the occurrence of straight crystallographically oriented dislocations and an inverse dependence of the strain rate sensitivity of the flow stress on the strain rate in the anomaly range, a new model was suggested for describing the anomalous increase of the flow stress. It is based on an idea by M. J. Mills et al. that the dislocations dissociate along certain crystallographic directions by glide into a nonplanar configuration which moves by a combination of glide and conservative climb. Such a mechanism may have the kinetics of the Cottrell effect.

– In the high-temperature range, the flow stress is controlled by recovery.

Acknowledgements The authors are very grateful to Prof. M. Yamaguchi, Kyoto University, for supplying the single crystal and for fruitful discussions. They also thank one of the referees of this paper for giving a hint at the dissociation reaction in Eq. (12). Financial support by the Deutsche Forschungsgemeinschaft (DFG) is gratefully acknowledged.

References

[1] Y. Umakoshi, T. Sakagami, T. Hirano, and T. Yamane, Acta Metall. Mater. **38**, 909 (1990).
[2] S. A. Maloy, A. H. Heuer, J. J. Lewandowski, and T. E. Mitchell, Acta Metall. Mater. **40**, 3159 (1992).
[3] S. A. Maloy, T. E. Mitchell, J. J. Lewandowski, and A. H. Heuer, Philos. Mag. Lett. **67**, 313 (1993).
[4] S. A. Maloy, T. E. Mitchell, and A. H. Heuer, Acta Metall. Mater. **43**, 657 (1995).
[5] K. Ito, H. Inui, S. Shirai, and M. Yamaguchi, Philos. Mag. A **72**, 1075 (1995).
[6] B. H. Kear and H. G. F. Wilsdorf, Trans. TME-AIME **224**, 382 (1962).
[7] S. Takeuchi and E. Kuramoto, Acta Metall. **21**, 415 (1973).
[8] V. Paidar, D. P. Pope, and V. Vitek, Acta Metall. **32**, 435 (1984).
[9] U. V. Waghmare, V. Bulatov, E. Kaxiras, and M. S. Duesbery, Philos. Mag. A **79**, 655 (1999).
[10] D. J. Evans, S. A. Court, P. M. Hazzledine, and H. L. Fraser, Philos. Mag. Lett. **67**, 331 (1993).
[11] H. Inui, K. Ishikawa, and M. Yamaguchi, Intermetallics **8**, 1131 (2000).
[12] M. Yoo, Mater. Res. Soc. Proc. **646**, N4.10.1 (2001).
[13] A. A. Sharif, A. Misra, and T. E. Mitchell, Mater. Sci. Eng. A **358**, 279 (2003).
[14] T. E. Mitchell, P. M. Anderson, M. I. Baskes, S. P. Chen, R. G. Hoagland, and A. Misra, Philos. Mag. **83**, 1329 (2003).
[15] A. H. Cottrell, Philos. Mag. **74**, 829 (1953).
[16] U. Messerschmidt, M. Bartsch, S. Guder, D. Häussler, R. Haushälter, and M. Yamaguchi, Intermetallics **6**, 729 (1998).

[17] S. Guder, M. Bartsch, M. Yamaguchi, and U. Messerschmidt, Mater. Sci. Eng. A **261**, 139 (1999).
[18] U. Messerschmidt, M. Bartsch, S. Guder, and D. Häussler, Mater. Res. Soc. Symp. Proc. **552**, KK10.9.1 (1999).
[19] S. Guder, PhD Thesis, Martin Luther University, Halle/Wittenberg (2000).
[20] U. Messerschmidt, S. Guder, D. Häussler, and M. Bartsch, Mater. Res. Soc. Symp. Proc. **652**, Y11.6.1. (2001).
[21] U. Messerschmidt, S. Guder, L. Junker, M. Bartsch, and M. Yamaguchi, Mater. Sci. Eng. A **319–321**, 342 (2001).
[22] M. J. Mills, R. Srinivasan, and M. S. Daw, Philos. Mag. A **77**, 801 (1998).
[23] T. E. Mitchell, M. I. Baskes, S. P. Chen, J. P. Hirth, and R. G. Hoagland, Philos. Mag. A **81**, 1079 (2001).
[24] U. Messerschmidt, M. Bartsch, and Ch. Dietzsch, The flow stress anomaly in Fe–43 at% Al single crystals, submitted to Intermetallics.
[25] U. Messerschmidt and M. Bartsch, Ultramicroscopy **56**, 163 (1994).
[26] T. E. Mitchell, J. P. Hirth and A. Misra, Acta Mater. **50**, 1087 (2002).
[27] R. K. Ham, Philos. Mag. **6**, 1183 (1961).
[28] M. Nakamura, S. Matsumoto, and T. Hirano, J. Mater. Sci. **25**, 3309 (1990).
[29] S. I. Rao, D. M. Dimiduk, and M. G. Mendiratta, Philos. Mag. A **68**, 1295 (1993).
[30] D. Baither, PC code for calculating dislocation line energy and tension in anisotropic elasticity theory (1999), unpublished.
[31] K. Tanaka, H. Onome, H. Inui, M. Yamaguchi, and M. Koiwa, Mater. Sci. Eng. A **239–240**, 188 (1997).
[32] A. Seeger, in: Handbuch der Physik, edited by S. Flügge (Springer-Verlag, Berlin, 1958), p. 1.
[33] G. I. Taylor, Proc. Roy. Soc. **145**, 362 (1934).
[34] B. V. Petukhov, M. Bartsch, and U. Messerschmidt, Eur. Phys. J. Appl. Phys. **9**, 89 (2000).
[35] J. P. Hirth and J. Lothe, Theory of dislocations (Wiley & Sons, New York, 1982).
[36] S. Guder, M. Bartsch, and U. Messerschmidt, Philos. Mag. A **82**, 2737 (2002).
[37] K. Ito, K. Matsuda, Y. Shirai, H. Inui, and M. Yamaguchi, Mater. Sci. Eng. A **261**, 99 (1999).
[38] T. E. Mitchell, M. I. Baskes, R. G. Hoagland, and A. Misra, Intermetallics **9**, 849 (2001).
[39] M. I. Baskes and R. G. Hoagland, Acta Mater. **49**, 2357 (2001).
[40] M. Salamon and H. Mehrer, Def. Diffusion Forum **216–217**, 161 (2003).
[41] M. Salamon, A. Strohm, T. Voss, P. Laitinen, I. Riimimäki, S. Divinski, W. Frank, J. Räisänen, and H. Mehrer, Philos. Mag. **84**, 737 (2004).
[42] X. Y. Zhang, W. Sprengel, T. E. M. Staab, H. Inui, and H.-E. Schaefer, Phys. Rev. Lett. **92**, 155502 (2004).
[43] W. R. Cannon and T. G. Langdon, J. Mater. Sci. **18**, 1 (1983).